Soft, stiffness-controllable sensing tip for on-demand force range adjustment with angled force direction identification

Duncan G. Raitt, Sara-Adela Abad, Shervanthi Homer-Vanniasinkam, and Helge A. Wurdemann.

***Abstract*— Force sensors are essential for measuring and controlling robot-object interactions. However, current force sensors have limited usability in applications such as grasping and palpation, where the range of angled forces changes between tasks. To address this limitation this paper proposes a novel optical-based soft-tipped force sensor capable of adjusting its range and sensitivity through pneumatic modulation. This research describes the sensor's design and examines the relationship between the internal pressure of the sensor and its sensing range, sensitivity, single-axis force-sensing accuracy, and capability of measuring the angle and magnitude of non-normal forces. Results indicate that by increasing the pressure in the sensor, the sensing range can be increased and the sensitivity decreased. These results demonstrate that the sensor can measure normal forces reliably at each pressure using 4th order fits with root-mean-square error (RMSE)$\in$ [0.032 N 0.110 N]. Finally, it is also demonstrated that by using a neural network, the sensor can measure the angle and magnitude of non-normal forces with RMSEs on trained variables of 0.0120 Rad for Y-angle (θ_Y) measurements, 0.0109 Rad for X-angle (θ_X) measurements, and 0.102 N for force measurements.**

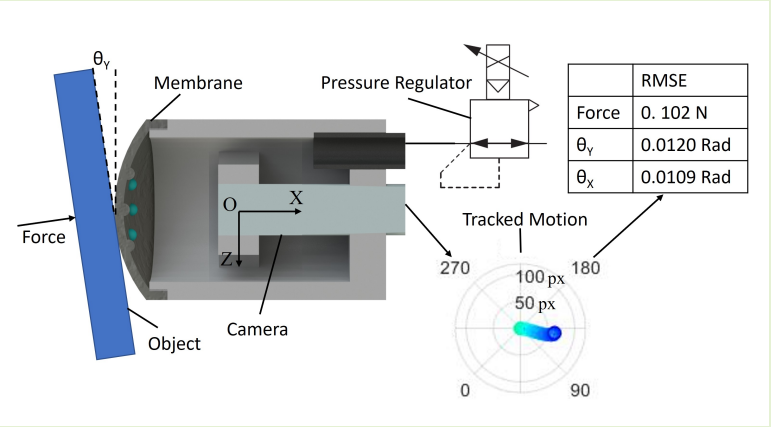

***Index Terms*— adjustable range, force sensor, neural network, soft sensor, variable stiffness**

I. Introduction

FORCE-SENSING is a key part of tactile sensing in robotics. Force sensors mounted on the tip of a mechanism gather information about interactions between the mechanism tip and other bodies. These devices can be found throughout the field of robotics, including in haptic grippers [1], [2], manufacturing tools [2], [3], and medical robotics [2], [4]–[6].

Traditionally, force-sensing is achieved by tracking the displacement of a hard-tipped device with known stiffness as it interacts with an object. Many technologies have been used to construct force-sensing tips, including force-sensitive resistors [7], capacitive-based sensing cells [8], [9], piezoresistive sensors [9], [10], fiber Bragg gratings [11]–[13] and optical deformation sensing [14].

Whilst most devices measure force on a solid tip interacting with an object, some devices measure the deformation of a soft membrane to find the applied force. This reduces damage to the object. There have been a number of soft sensors produced, using sensing methods such as, optical sensing [15], [16], giant magnetoresistance [17], hall effect sensing [18], [19] and inductance [20]. Whilst many of these papers do not address the sensor's accuracy, those that do have average errors and root-mean-square errors (RMSE) for flat normal force sensing ranging from 5% to 10% of the sensor's range [16], [17]. To adjust the range of any of these sensors requires them to be reconstructed with different materials or geometry. This restricts the applications they can be used in as they are not able to quickly adapt to the changing force range that may be required in a dynamic task.

To solve this issue and make soft force sensors more adaptable, researchers have been looking into variable stiffness soft force sensors. For example, Gaudeni et al. produced a mathematical model for deriving force from pressure change in a small pneumatic balloon with a known inflating pressure and radius at that pressure [21]. This model was validated with the manual pushing of the inflated balloon against a hard flat ATI F/T sensor. Results showed a mean error of 9.14%

This work was supported by the UK Engineering and Physical Sciences Research Council (EPSRC) under grant EP/S014039/1 and the UCL Department of Mechanical Engineering.

All authors are with the Department of Mechanical Engineering, UCL, London, WC1E 7JE, UK. (e-mail: {duncan.raitt.19, s.abad-guaman, s.homer-v, h.wurdemann}@ucl.ac.uk).

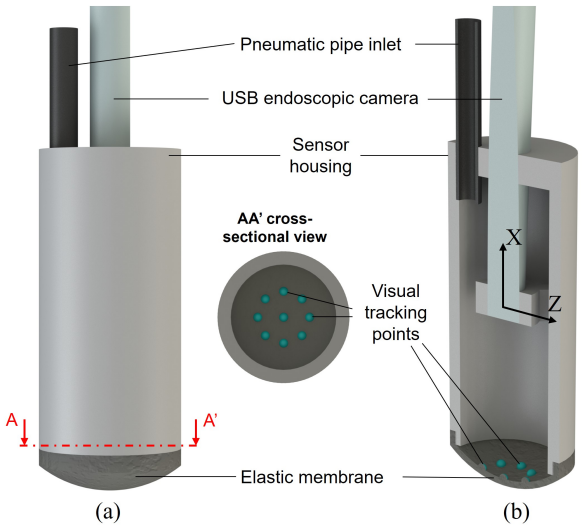

Fig. 1. (a) Side view and (b) 3D cross-sectional view of our proposed sensor with variable force range and sensitivity through a pneumatically pressurized elastic membrane. An integrated visual camera tracks points on the inner surface of the membrane that will be displaced during deformation.

in calculating peak force. The range and sensitivity of this device may be adjustable by varying the pressure, however, this has not been investigated, and the mathematical model cannot measure the angle of non-normal forces.

In line with this approach, Zhang et al. developed a variable stiffness force sensor [22]. This sensor uses a 3D hall effect sensor to measure normal forces and can adjust its range and sensitivity by changing its internal pressure. It was tested using several materials with a wide and narrow indenter over a pressure range of 0 to 27.5 kPa; a genetic program was trained to fit the data to intermediate pressures. This sensor was only tested with normal forces, and the variability and accuracy of the sensor were not analyzed.

Parallel with this, in previous work, we produced a 3D printed variable stiffness force sensor [23]. This sensor measures normal forces using a camera to measure the displacement of tracking points on an air pressurized membrane. The range and sensitivity of the sensor can be adjusted by changing its internal pressure. Regression analysis of a second-order fit on one of the sensor's outer tracking points demonstrated an average R^2 of 0.956 and an average RMSE of 0.13 N (5.8% of average range). Whilst these soft-tipped devices can vary their range, they have not been shown to measure non-normal forces. This prevents them from being used in applications were contact at different angles may occur.

In related research, Bewley et al. used a Tactip sensor with an adjustable internal pressure to detect small surface and embedded lumps within a silicone matrix [24], demonstrating that increasing the sensor pressure allowed deeper lumps to be detected more accurately. This sensor has a similar design and function to the sensor developed in this paper and our previous research, illustrating the large range of applications for which this sensor type can be used.

In this paper, we present an optical-based soft-tipped sensor

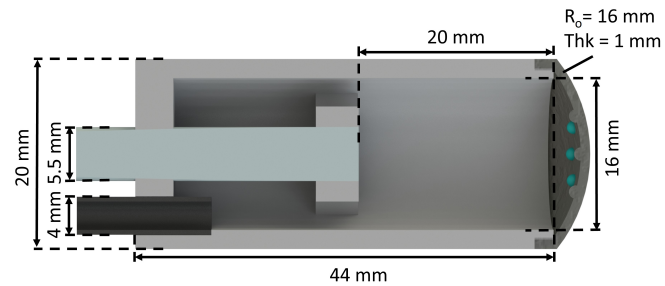

Fig. 2. Dimensions and cross-sectional view of the PMOT sensor where the camera is highlighted in blue.

that can measure the angle and magnitude of forces, and adjust its range using stiffness control. To do this, we build on our previous work [23] to produce a sensor that can measure non-normal forces. This sensor is referred to as a pressure modulated optical tracking (PMOT) force sensor. The PMOT sensor uniquely combines the use of a pressurizable sealed chamber with a deformable membrane covered with low lying tracking points that are tracked by a camera. This enables it to vary its stiffness through pressurization and measure deformations of the membrane at different locations. These advantages allow it to be used in tasks where the force range of angled forces may change between tasks such as palpation and gripping different objects.

This paper aims to:

1) present the sensing principle, design, and fabrication process of the sensor.
2) demonstrate experimentally that the PMOT sensor can measure the magnitude of normal forces using a polynomial fit, and show that the range and sensitivity of the sensor can be adjusted by changing the internal pressure of the sensor.
3) prove with experiments that, using a neural network, the sensor can measure the angle and magnitude of non-normal forces at different internal pressures.

II. Sensing Principle and Mechanical Design

A. Sensing Principle

The PMOT force sensor measures the deformation of a pressurized elastomer membrane under force loads. By varying the stiffness of the membrane, the range and sensitivity of the sensor can be controlled. The stiffness of the sensor increases with pressure due to two main factors. Firstly, the increase of the internal pressure causes the internal air mass to rise in line with the ideal gas equation, leading to an increase in internal stiffness [25]. Secondly, the membrane increases in strain as the internal pressure grows, causing the membrane to stiffen. Additionally, increasing the internal pressure of the sensor increases the initial inflation height of the membrane, further increasing the range of the sensor.

B. Mechanical Design and Fabrication

The PMOT force sensor and its internal components are shown in Fig. 1, whilst Fig. 2 shows a cross-sectional view and its dimensions.

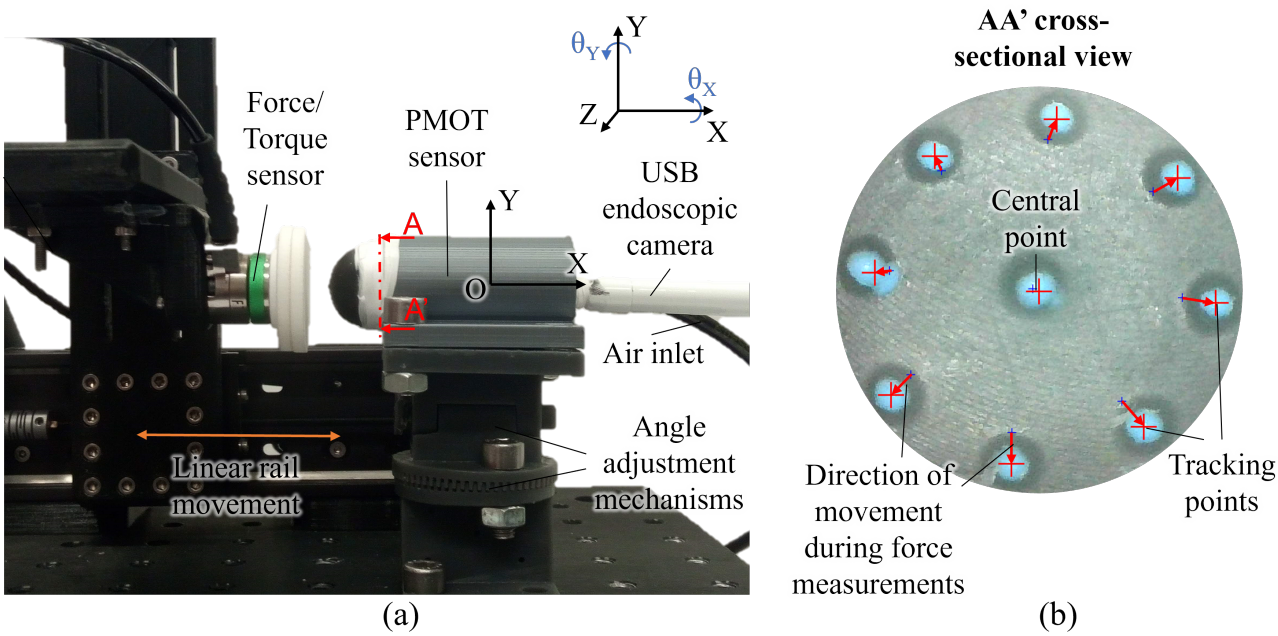

Fig. 3. (a) Experimental setup: A Force/Torque sensor mounted on a robotized linear rail exerts forces on the elastic membrane of our sensor prototype. As a result, (b) the projected locations of the tracking points are visually monitored and analyzed.

The PMOT sensor housing was produced from Formlabs Tough 2000 and printed on a Form 3 printer. The outer diameter of the housing is 20 mm with an inner diameter of 16 mm. The membrane is attached at the distal end of the housing. In our previous work, the membrane was 3D printed with plastic tracking points to ensure fast and reproducible fabrication with adaptable geometry. In this paper, the membrane is cast from a platinum catalysed silicone elastomer . This allows the membrane to be more robust and isotropic, whilst providing more choices in membrane stiffness and reducing reflections. The dome-shaped membrane with an outer dome radius of 16 mm and a thickness of 1 mm was cast from Ecoflex 00-30. The Ecoflex was mixed with a ratio of 5 g part A to 5 g part B, into which two drops of Silc Pig black was added to make the membrane black. This mixture was poured into casting moulds and degassed. The membrane is covered in nine 0.7 mm radius tracking points arranged with one in the centre and eight in a circle with a radius of 4 mm. The tracking points are painted with cyan to ensure they can be tracked by the camera. Where the membrane meets the housing, it has an outer diameter of 20 mm, an inner diameter of 18 mm, and overlaps the housing by 2 mm. The membrane is glued and taped to the housing to ensure a strong, airtight seal.

Holes in the housing are used to insert the pneumatic piping and a USB endoscopic camera. The 4 mm diameter pneumatic piping, shown in Fig. 2, is connected to a pressure regulator used to control the pressurisation of the membrane. The 1.3 MP camera measures 5.5 mm in diameter and is held halfway down the housing to increase its stability during measurement; it is positioned with the lens 20 mm from the end of the housing. This camera captures the location of the tracking points.

Data from the camera is fed to a computer that calculates and records the position of the centre of each tracking point. This is done using a set of commands in the OpenCV library [26]. A colour mask is used to segment the tracking points, Canny edge detection with a threshold of 80 detects and isolates boundaries, and a find contours algorithm extracts borders from the boundaries. The displacements of the tracking points in the camera image are a projection of the tracking points movements in all three dimensions projected onto a plane.

III. Methodologies

Two experiments were carried out to assess the performance of the sensor. Experiment 1 tested the normal force sensing accuracy and reliability of the sensor, and analyzed how the sensor's internal pressure affected its range and sensitivity.

- The sensor is pressed at different normal forces against an F/T sensor by a linear rail.
- The displacement of the tracking points is recorded as the sensor input.
- The Force data from the F/T sensor is extracted as a ground truth for training and testing.
- The internal pressure of the sensor is varied between experiments.

Experiment 2 assessed the sensor's ability to measure the angle and magnitude of non-normal forces at different internal pressures using a neural network.

- The sensor is pressed at different forces against an F/T sensor by a linear rail.
- The displacement of the tracking points and pressure is recorded as the sensor input.

- The Force data from the F/T sensor and angles of contact are extracted as a ground truths for training, validation and testing.
- The internal pressure of the sensor and the angle of contact is varied between experiments.
- A neural network is used to establish the relationships between the sensor inputs and ground truths.

A. Experiment 1: Normal Force Sensing Methodology

This experiment was designed to obtain the tracking points' positions and displacements in Cartesian coordinates from the PMOT sensor camera, and the force in Newton (N), measured with a IIT-FT17 F/T sensor during loading and unloading of the membrane. The PMOT sensor was mounted on a platform opposite the F/T sensor on a linear rail. These were positioned so that as the F/T sensor was brought into contact with the membrane, it would remain parallel to, and concentric with, the membrane. F/T sensors mounted on linear rails are commonly used to calibrate and validate force sensors as they allow multiple forces to be automatically tested in quick succession [12]–[14], [17]. Our experiments were run in line with these previous works with only minor variations for the sensors range and sensing process. The diameter of the F/T sensor was larger than the membrane ensuring complete and flat contact. This setup is shown in Fig. 3.

The F/T sensor was set to its home position 20 mm from the membrane. The PMOT sensor was pressurized to the required pressure. The linear rail then moved the F/T sensor towards the membrane until the contact force surpassed 0.2 N. The F/T sensor was moved back 3 mm to ensure no contact was made prior to sampling. Following this, the linear rail was moved in 0.1 mm steps towards the PMOT sensor. The rail stopped for 1 s at each step to allow the membrane to adjust, then the force and tracking point locations were sampled 5 times, with a 0.2 s gap between samples. Steps were repeated until the F/T sensor had moved 12 mm or the force became greater than 5 N. Following this, steps and sampling were repeated, moving away from the PMOT sensor until the F/T sensor reached its starting position.

This experiment was repeated 15 times per pressure at internal pressures of 2, 4, and 6 kPa. Ten tests were designated as training data whilst five tests were designated as testing data. Three priming runs of the experiment were carried out whenever the experiment was set up; these results were discarded. Internal pressures of up to 6 kPa were chosen to avoid the sensor approaching the pressure limit of the membrane-housing bond (10 kPa) even with large pressure variations, and to avoid the tracking points leaving the view of the camera, which was observed at 8 kPa.

Data was extracted and processed for each point at each pressure during loading and unloading. Tracking point data was converted to polar coordinates around the central point to find the radial displacement (Δr) in pixels (px) and angular displacement ($\Delta\theta$) in degrees (°) of the tracking points. Δr measures the tracking point's change in distance from the centre point whilst $\Delta\theta$ measures the change in angular displacement around a circumference with an origin at the central point. This allows the direction and displacement of the tracking points' movements to be assessed whilst also allowing the effects of torsion on the membrane to be removed. The average radial displacement ($\overline{\Delta r}$) was obtained by averaging the Δr for all tracking points at each measurement.

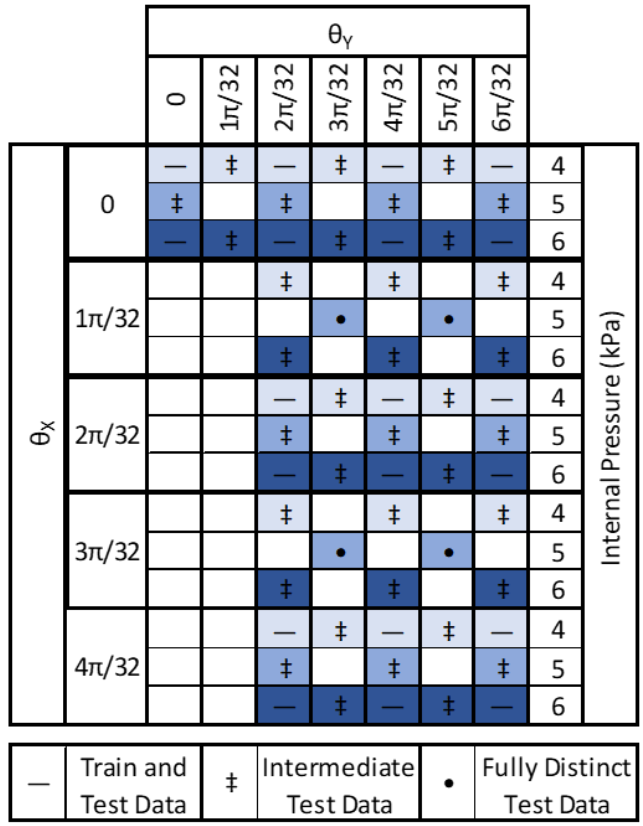

Fig. 4. Matrix showing the combinations of Y-angles, X-angles, and internal pressures used for training and testing, for intermediate test sets, and for fully distinct test sets.

B. Experiment 2: Angled Force Sensing Methodology

The experiment in Subsection III-A was repeated with the sensor rotated around the Y-axis and X-axis as shown in Fig. 3. The experiment was carried out with Y-angles (θ_Y) of 0, $2\pi/32$, $4\pi/32$ and $6\pi/32$ radians (Rad), X-angles (θ_X) of 0, $2\pi/32$ and $4\pi/32$ Rad, internal pressures of 4 and 6 kPa, and combinations of these parameters. These were all repeated 17 times. The entire data set was divided into three groups: ten repetitions were used for training, two were used for verification, setting the hyper-parameters and selecting a model, and five were used for testing. It should be noted that when there is no rotation around the Y-axis, i.e., contact is normal to the sensor, rotating the sensor around the X-axis produces no variation in output and could, therefore, not be used as training data.

A θ_Y range of $6\pi/32$ Rad was chosen because after this point the F/T sensor makes insufficient contact with the sensor to be processed when the internal pressure is 4 kPa. A θ_X range of $4\pi/32$ Rad was chosen as the tracking points are placed radially symmetrical at intervals of $8\pi/32$ Rad with an axis of symmetry between them. This means that results

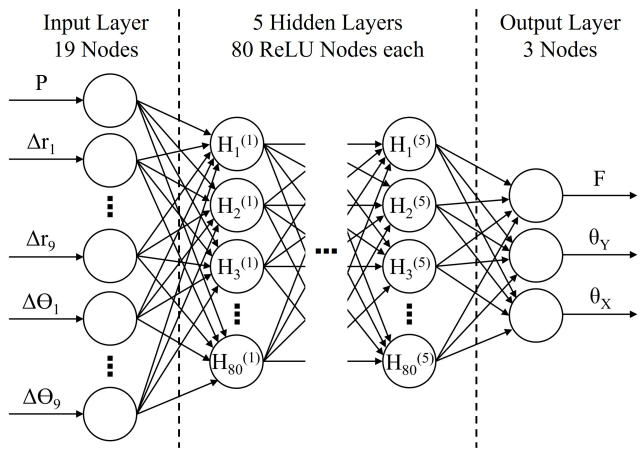

Fig. 5. Neural network architecture showing inputs, nodes and outputs.

within a range of $4\pi/32$ Rad can be extrapolated to contact at any θ_X.

On top of this, the experiment was repeated with intermediate variables for testing, paired with all trained variables. These were: θ_Y of $\pi/32$, $3\pi/32$ and $5\pi/32$ Rad, θ_X of $\pi/32$ and $3\pi/32$ Rad, and an internal pressure of 5 kPa. These intermediate variables were also paired with each other to produce fully distinct training data. Each combination was repeated five times. Fig. 4 shows all combinations of variables used in this experiment, denoting if the combinations were were used for training and testing, for intermediate test sets, or to produce fully distinct test data.

All data below 0.05 N and above the range at each pressure obtained in the normal force-sensing results were removed. This was because the angle of contact would have no effect prior to contact and at negligible forces, and the deformation of the membrane does not correlate to force after contact with the housing. For angled force-sensing analysis, tracking point data was transferred to polar coordinates around each tracking point's initial position with the reference direction pointing away from the centre point. This allows the motion of individual tracking points to be monitored and compared more easily. The pressure (P) in kPa, and the radial displacement (Δr) in px and angular displacement ($\Delta\theta$) in $^\circ$ for each tracking point were exported as sensor inputs. Whilst the Force (F) in N, and contact angles (θ_Y) and (θ_X) in Rad were exported as expected outputs. This experiment produced 6465 lines of training data, 1383 lines of validation data, and 7657 lines of test data.

IV. Neural Network Architecture

Data from Experiment 2 was processed using a multi-output regression deep neural network. Neural networks have started to be used for force sensing when the relationships between inputs are too complex for traditional mathematical algorithms [27]–[29]. All data was standardized and shuffled before being processed, and the network used an Adam optimization algorithm. The validation data was used to select the algorithm architecture. The final architecture, shown in Fig. 5, consisted of five hidden layers with 80 nodes each.

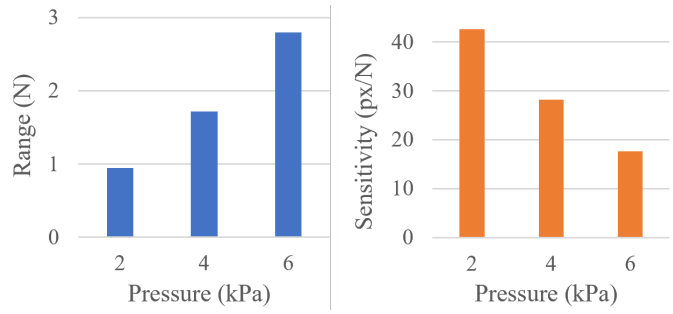

Fig. 6. Sensitivity and range with different internal pressures. It demonstrates that as internal pressure is increased, range increases whilst sensitivity decreases.

All nodes used a Rectified Linear Unit (ReLU) activation function. The algorithm was trained for 100 epochs and was compared to the validation data every 50 iterations. The output network was selected as the network that performed best with the validation data.

V. Results

A. Experiment 1: Normal Force Sensing Results

The results from Experiment 1 were analyzed in three steps. Firstly, the change in the sensor's range and sensitivity with internal pressure was examined. Secondly, the performance of the sensor was assessed using the training data, and the sensor parameters were obtained. Finally, testing data was used to evaluate the accuracy of the sensor.

The average $\Delta\theta$ across all points, internal pressures, and forces was 0.008°, showing negligible torsional effects. Therefore, only Δr will be analyzed in the results.

1) Inter-Pressure Results: Training data was compared between internal pressures to examine how changing the internal pressure of the PMOT sensor affected the sensitivity and range of the sensor. This was done by comparing force data to $\overline{\Delta r}$ between pressures, combining all experiments

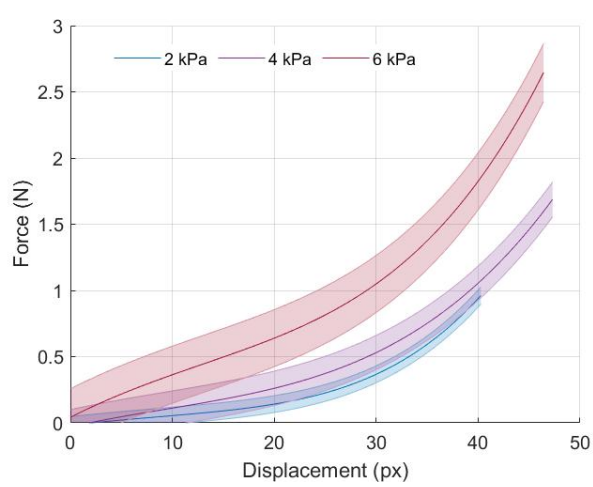

Fig. 7. Force-displacement 4th order fit at each pressure with confidence intervals. At each pressure, a single value of displacement corresponds to a single value of force. Further, it is demonstrated that the sensitivity at each pressure decreases across its sensing range.

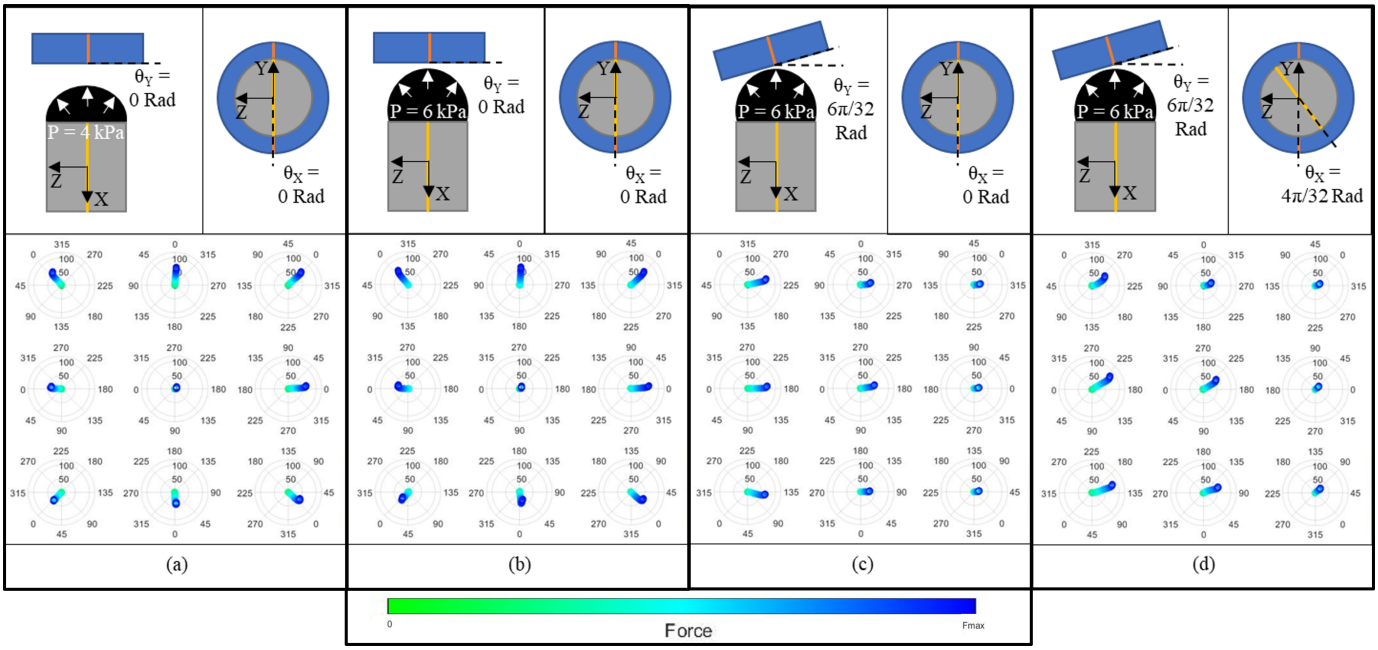

Fig. 8. Visual data analysis of angled force sensing data. Graphs show how the polar coordinates of all nine tracking points, with the reference direction pointing away from the centre point, change with force. These are compared amongst changes in pressure P, contact $\boldsymbol{\theta_Y}$, and contact $\boldsymbol{\theta_X}$. (a) P = 4 kPa, $\boldsymbol{\theta_Y}$ = 0 Rad, $\boldsymbol{\theta_X}$ = 0 Rad. (b) P = 6 kPa, $\boldsymbol{\theta_Y}$ = 0 Rad, $\boldsymbol{\theta_X}$ = 0 Rad. (c) P = 6 kPa, $\boldsymbol{\theta_Y}$ = $\boldsymbol{6\pi/32}$ Rad, $\boldsymbol{\theta_X}$ = 0 Rad. (d) P = 6 kPa, $\boldsymbol{\theta_Y}$ = $\boldsymbol{6\pi/32}$ Rad, $\boldsymbol{\theta_X}$ = $\boldsymbol{4\pi/32}$ Rad.

during loading and unloading. The range of the sensor at each pressure was taken to be the force reading before the membrane was pushed against the housing during loading testing. This was determined as the point in the latter half of the loading data, where the change in force with linear rail displacement exceeded six times the average gradient from all preceding samples. A best fit straight line is used to find the sensitivity of the device at each pressure. The sensitivity and range of the sensor at each pressure are compared in Fig. 6.

2) Performance Analysis Results: The training data was fitted to a polynomial, and the goodness of fit was analyzed. The performance of the sensor was further analyzed using training data fits to find the sensor parameters.

From the training data, force against $\overline{\Delta r}$ was fitted to a 4th order polynomial at each internal pressure. A 4th order polynomial was chosen as it produced the highest average coefficient of determination (adjusted R^2) across all training data when compared to all other polynomials up to 6th order. The goodness of fit and data variability was analyzed through regression analysis to compare the fits to training data points over the range shown in Fig. 6. Table I shows the adjusted R^2 and RMSE in Newtons, and as a percentage of the range, for the fits at each pressure. The 4th order fits and 95% confidence intervals for each internal pressure are shown in Fig. 7. Although a 4th order fit was used, each value of displacement correlates to only a single value of force. Furthermore, the results demonstrate that the sensitivity decreases as the force increases at each pressure. To analyze the sensor function, sensor parameters are calculated. These sensor parameters are summarized in Table II. The inter-point root-mean-square deviation (RMSD) was analyzed by comparing the Δr of each tracking point to $\overline{\Delta r}$ at all data points over each experiment. The mean and standard deviation (SD) of these values for each pressure was calculated. This was compared to the sensors maximum output to obtain the deviation as a percentage.

The non-repeatability was obtained by measuring the maximum difference between readings at the same sample, and the maximum value for each pressure was extracted from all samples in all experiments. This was compared to the sensor's maximum output to obtain the non-repeatability as a percentage.

Hysteresis was obtained by fitting 6th order polynomials to loading and unloading data separately; the difference between these fits were obtained at 0.1 N intervals over their ranges shown in Fig. 6, and the maximum difference for each experiment was recorded. The mean and SD of these values for each pressure was calculated. These were also compared to the sensor's maximum output to obtain the hysteresis as a

TABLE I
NORMAL FORCE SENSING VARIABILITY

	Internal Pressure		
	2 kPa	4 kPa	6 kPa
∂_4 Adjusted R^2	0.981	0.978	0.974
∂_4 RMSE (N)	0.0322	0.0659	0.1097
∂_4 RMSE (%)	3.41	3.84	3.92

TABLE II
NORMAL FORCE SENSING PARAMETERS

		Internal Pressure		
		2 kPa	4 kPa	6 kPa
Inter-point Deviation	(Mean RMSD %)	13.1	13.0	15.4
	(SD RMSD %)	0.325	0.303	0.507
Non-repeatability	(%)	10.37	9.39	9.95
Hysteresis	(Mean %)	7.44	8.57	11.05
	(SD %)	1.273	1.737	0.748

TABLE III
NORMAL FORCE SENSING TEST DATA RESULTS

		Internal Pressure		
		2 kPa	4 kPa	6 kPa
Accuracy	(RMSE N)	0.0342	0.0611	0.1220
	(RMSE %)	3.63	3.56	4.36
	(Max Error %)	26.2	17.9	21.8

TABLE IV
ANGLED SENSING NETWORK ACCURACY

	Trained Variables	Intermediate Pressures	Intermediate θ_Y	Intermediate θ_X	Fully Intermediate
Force (N)	0.102	0.297	0.320	0.226	0.398
RMSE (%)	3.64	10.61	11.43	8.08	14.22
θ_Y (Rad)	0.0120	0.0188	0.0410	0.0202	0.0570
RMSE (%)	2.04	3.19	6.96	3.43	9.68
θ_X (Rad)	0.0109	0.0162	0.0300	0.0500	0.0472
RMSE (%)	2.78	4.13	7.64	12.73	12.02

percentage.

3) Test Data Results: Sensor accuracy was assessed by comparing test data to the 4th order polynomials fit obtained from the training data. The RMSE and maximum error in Newtons and as a percentage of the range were obtained; these results are shown in Table III.

B. Experiment 2: Angled Force Sensing Results

1) Visual Data Analysis: Data was first visually analyzed to spot trends before training the neural network. In Fig. 8, graphs show how the position of each tracking point changes with force. A diagram above each graph shows the variable that is altered between each graph; these variables are the internal pressure and the θ_Y and θ_X of contact. There is a clear difference in tracking point displacement with force when the pressure of the sensor, or the θ_Y or θ_X of the force, are adjusted.

2) Overall Neural Network Results: The data was then combined and fed into the neural network as described in Section IV. The accuracy of the network was obtained by comparing the network's predicted outputs to those recorded in the experiment for the trained variables and for each set of intermediate variables, and calculating the RMSE. These are shown in Table IV both in Newtons and radians, and as a percentage of their range. The range of force was the same as that shown in Fig. 6 at 6 kPa, whilst the ranges for θ_Y and θ_X sensing were taken to be $6\pi/32$ and $4\pi/32$ respectively. The errors in each measurement vary between data sets. Across all data the RMSEs for Force, θ_Y and θ_X were 0.2760 N, 0.0310 Rad and 0.0328 Rad respectively, or 9.86%, 5.26% and 8.35% of their respective ranges.

3) Performance Analysis: To further understand where the errors were occurring in the angle measurements, confusion matrices were produced. These show the value predicted by the neural network, rounded to the nearest $\pi/32$, as a percentage of data-points at each true value. These are shown in Table V. Table VI compares the errors obtained at high and low forces and at high and low angles to determine if there is any correlation. The low and high force divide was set to 1 N as this is half of the range at an internal pressure of 4 kPa.

TABLE V
CONFUSION MATRIX OF ALL ANGLE SENSING TEST DATA. THIS SHOWS THE TRUE VALUE OF THE TEST DATA COMPARED TO THE PREDICTED VALUE FROM THE NEURAL NETWORK, ROUNDED TO THE NEAREST $\pi/32$. (A) SHOWS θ_Y PREDICTION RATE AND (B) SHOWS θ_X PREDICTION RATE. ALL VALUES ARE GIVEN AS A PERCENTAGE OF THE TOTAL NUMBER OF DATA POINTS FOR THAT TRUE VALUE.

True Value \ Predicted value	0.0	1π/32	2π/32	3π/32	4π/32	5π/32	6π/32
0.0	98.0	1.7	0.0	0.3	0.0	0.0	0.0
1π/32	24.2	65.5	7.9	2.5	0.0	0.0	0.0
2π/32	0.0	0.6	98.9	0.5	0.0	0.0	0.0
3π/32	0.1	0.0	41.3	58.6	0.0	0.0	0.0
4π/32	0.0	0.2	0.0	1.5	98.0	0.3	0.0
5π/32	0.0	0.0	0.0	0.0	0.2	97.7	2.0
6π/32	0.0	0.0	0.0	0.0	0.0	0.7	99.3

(a)

True Value \ Predicted value	0.0	1π/32	2π/32	3π/32	4π/32
0.0	97.3	2.5	0.2	0.0	0.0
1π/32	12.7	71.3	15.7	0.3	0.0
2π/32	0.4	0.4	85.7	13.5	0.0
3π/32	0.3	0.0	36.3	59.9	3.6
4π/32	0.0	0.0	0.1	1.7	98.2

(b)

TABLE VI
RELATIONSHIP BETWEEN ERRORS IN EACH VARIABLE, AND THE MAGNITUDE AND θ_Y OF THE FORCE

	Low θ_Y (0 - $2\pi/32$ Rad)	High θ_Y ($4\pi/32$ - $6\pi/32$ Rad)	
n	2385	2340	Low Force ($<$ 1 N)
Force RMSE (N)	0.108	0.239	
θ_Y RMSE (Rad)	0.0295	0.0213	
θ_X RMSE (Rad)	0.0378	0.0253	
n	881	584	High Force ($>$ 1 N)
Force RMSE (N)	0.450	0.376	
θ_Y RMSE (Rad)	0.0175	0.0144	
θ_X RMSE (Rad)	0.0253	0.0196	

TABLE VII
ANGLED SENSING ACCURACY WITH PRESSURE

	Internal Pressure	
	4 kPa	6 kPa
Force RMSE (N)	0.170	0.287
θ_Y RMSE (Rad)	0.0270	0.0317
θ_X RMSE (Rad)	0.0302	0.0370

T-tests of absolute errors were used to assess the significance of each of the relationships in Table VI. Errors in force sensing were significantly higher at high θ_Y than at low θ_Y, $t(6188) = 5.14$, $p < 0.001$, and significantly higher at high forces than at low forces, $t(6188) = 29.8$, $p < 0.001$. Errors in θ_Y sensing were significantly higher at low θ_Y than at high θ_Y, $t(6188) = 2.03$, $p = 0.04$, and significantly higher at low forces than at high forces, $t(6188) = 10.4$, $p < 0.001$. Errors in θ_X sensing were significantly higher at low θ_Y than at high θ_Y, $t(6188) = 7.18$, $p < 0.001$, and significantly higher at low forces than at high forces, $t(6188) = 8.48$, $p < 0.001$.

Results were analysed between 4 kPa and 6 kPa internal pressure as shown in Table VII. This shows higher errors in every variable at 6 kPa than at 4 kPa. T-tests of absolute errors in each variable between pressures showed that errors in force and θ_X sensing were significantly higher at 6 kPa than at 4 kPa, $t(5413) = 5.47$, $p < 0.001$ & $t(5413) = 4.62$, $p < 0.001$. However, differences in errors in θ_Y sensing with pressure were not significant, $t(5413) = 0.126$, $p = 0.900$.

VI. Discussion

A. Experiment 1: Normal Force Sensing Discussion

Inter-pressure results show that increasing the pressure of the sensor caused the range of the sensor to rise (0.943 N to 2.799 N) and the sensitivity of the sensor to fall (42.6 px/N to 17.7 px/N). This is illustrated in Figs. 6 and 7. The larger range of the sensor is due to the sensor stiffening as the internal pressure is increased.

Results in Table I showed an average R^2 of 0.978 and an average RMSE of 0.069 N or 3.69% of range, over all pressures. These results show that the change in $\overline{\Delta r}$ with force can be fitted well with a 4th order polynomial and that there is low variance between samples and experiments. Likewise, as the pressure, and therefore the range of the sensor, increased, the RMSE also increased (0.0322 N to 0.1097 N) and the R^2 decreased (0.981 to 0.974).

Sensor parameters, shown in Table II, demonstrated the sources of errors in the sensor. Inter-point deviation shows the asymmetries in the device caused by fabrication or errors caused by imperfect experimental setup. Results showed an average RMSD between points of 13.8% of range. These deviations may be due to imperfections in the alignment of the lens or sensor in the camera, alignment of the camera in the housing, casting of the membrane, painting of the tracking points, gluing or taping of the membrane to the housing, or alignment of the membrane and the F/T sensor. These errors are removed by combining displacements into $\overline{\Delta r}$ in experiment 1 and by training each point separately in experiment 2. Improving fabrication methods such as using a more accurately aligned camera and producing a jig for colouring the tracking points would allow for fewer errors. However, these would increase the cost of manufacturing the sensor.

Non-repeatability shows the maximum difference in sensor reading in the exact same conditions. Results, averaging 9.95% of range, demonstrate that it is beneficial to take multiple readings when measuring force.

Hysteresis shows the maximum difference between loading and unloading data. The hysteresis readings, averaging 9.02% of range, are likely due to the elastic properties of the membrane. Changing the material of the membrane may decrease the hysteresis.

Test data results in Table III confirm that the fit works on non-trained data to measure the force with an accuracy, measured as the average RMSE, of 3.85% of range. These errors are lower than other soft sensors covered in this paper [16], [17], [21]. These results also verify that by increasing the internal pressure of the sensor, the RMSE in N is increased (0.0342 N to 0.1220 N), corresponding to the decreased sensitivity. Max errors, averaging 22.0% of range, show that readings should be verified with multiple measurements.

B. Experiment 2: Angles Force Sensing Discussion

Visual data analysis (Fig. 8) showed variation between force and tracking point location. As the internal pressure was increased from 4 kPa in Fig. 8-a to 6 kPa in Fig. 8 b, higher forces were required to produce the same tracking point displacement. In Fig. 8-c and d, the path the tracking point moves with force is altered as the Y-angle and X-angle were changed. At the high angles used in visualisation (Fig. 8-c and d), the tracking points close to where the force was applied move away from this location, whilst the tracking points on the other side of the sensor do not move. This aspect allows us to visually assess where the force is coming from. These results suggest that an algorithm should be able to relate internal pressure and tracking point locations to the angle and magnitude of a force.

Visual data analysis was confirmed in the overall neural network results, which showed that the direction and magnitude of force could be measured by the sensor using a neural network. The highest accuracy , RMSEs for Force, θ_Y and θ_X of 0.102 N, 0.0120 Rad and 0.0109 Rad respectively, was achieved in data sets where the conditions were similar to training data sets (Table IV). A high correlation could be seen between the type of untrained data introduced and the errors resulting from it. Intermediate θ_Y produced the highest errors in θ_Y sensing and intermediate θ_X produced the highest errors in θ_X sensing. Force sensing errors were high with intermediate pressures and intermediate θ_Y. Fully intermediate data had the highest errors in force and θ_Y sensing, and the second-highest errors in θ_X sensing. Increasing the spread of training variables would reduce the difference between trained and intermediate variables, thereby reducing the errors in intermediate variable sensing towards those of trained variables. The average force sensing RMSE of 9.86% of range is in line with other soft sensors covered in this paper [16], [17], [21].

The confusion matrices show where the errors in force sensing are large enough to be close to another tested angle. These further demonstrate lower errors in trained variable sensing, even when paired with other untrained variables, with all trained values having true positive values above 85%. Further analysis for tests with a θ_Y of $3\pi/32$, where the lowest

true positive value was observed showed an RMSE of 0.0511 Rad. Comparing this to the difference between tested angles of 0.0982 Rad, the RMSE is more than half of the difference between the angles, leading to the results shown in Table V. However, this error is still low compared to the angle between tracking points of 0.7854 Rad, showing that the accuracy of the sensor is not limited to the spacing of the tracking points. The confusion matrices also show that intermediate values tend to be underestimated for rotation around both axes; this suggests a non-linear relationship that may not be captured in the model.

Based on the results, Table IV and the T-tests demonstrate that increasing the angle or magnitude of the force alters the accuracy of measurements. The force measurements become less accurate in line with the results seen in Fig. 7 which shows higher sensitivity with low force. Meanwhile, the X- and Y-angle measurements become more accurate in line with Fig. 8, which shows less correlation between θ_Y and θ_X and tracking point displacement at low forces.

The analysis of angled sensing accuracy with pressure, Table VII and the T-tests align the results from experiment 1. This reinforces that increasing the stiffness of the sensor, decreases its force sensing accuracy. This was further shown to extend to a decrease in θ_X sensing accuracy .

VII. Conclusion and Future Work

This paper presented an optical-based soft-tipped sensor for measuring the angle and magnitude of forces with a range that is adjustable through stiffness control. We demonstrated the viability of the PMOT sensor for adjustable single-axis force-sensing via experiments and showed its ability to measure the angle and magnitude of non-normal forces at different internal pressures.

Normal force-sensing results showed that the range and sensitivity of the sensor could be controlled by adjusting the sensor's internal pressure. The range could be varied between 0.943 and 2.799 N. Using a 4th order fit allowed the sensor to measure forces with an accuracy (RMSE) of 0.032 to 0.110 N. Additionally, some errors in force sensing are mitigated through the sensing procedure whilst the others may be decreased by investigating changes to sensor materials and fabrication. The sensor uses a neural network to measure the angle and magnitude of a force. RMSEs of 0.102 N for force measurement, 0.0120 Rad for θ_Y measurement, and 0.0109 Rad for θ_X measurement were achieved on trained data. Demonstrating that the sensor can measure angles much lower than the angles between tracking points. The accuracy of measurements decreased when untrained data was introduced; this effect could be reduced by increasing the spread of training data.

Overall, the results shown in this paper demonstrate that this force sensor can be used in a wide range of applications due to its unique combination of attributes. The soft membrane allows the sensor to interact with objects without damaging them. The dynamically adjustable range allows the sensor to preform well in operations where the load ranges may vary within or between tasks. Additionally, the ability of the sensor to measure angles allows it to be used in applications with diverse angles of contact and where knowing the angle of contact is beneficial, such as in palpation and object manipulation in grippers. In future work, the sensor's ability to measure shear and torsional forces will be evaluated, and the sensor will be tested in application settings, such as palpation. An analysis will also be carried out about how the membrane material affects the performance and range of the sensor. The sensor behaviour will be analyzed when the pressure is changed during contact with an object in line with [30], and the dynamic characteristics of the sensor will be examined through cyclic loading and pressurisation.

Acknowledgment

We thank the Department of Mechanical Engineering, University College London for providing a PhD scholarship.

References

[1] C. Melchiorri, L. Moriello, G. Palli, and U. Scarcia, "A new force/torque sensor for robotic applications based on optoelectronic components," in *IEEE International Conference on Robotics and Automation*, 2014, pp. 6408–6413.

[2] Q. Liang, K. Zou, J. Long, J. Jin, D. Zhang, G. Coppola, W. Sun, Y. Wang, and Y. Ge, "Multi-component fbg-based force sensing systems by comparison with other sensing technologies: A review," *IEEE Sensors Journal*, vol. 18, no. 18, pp. 7345–7357, 2018.

[3] Y. Zhao, Y. Zhao, and X. Ge, "The development of a triaxial cutting force sensor based on a mems strain gauge," *Micromachines*, vol. 9, no. 1, 2018.

[4] A. L. Trejos, R. V. Patel, and M. D. Naish, "Force sensing and its application in minimally invasive surgery and therapy: A survey," *Proceedings of the Institution of Mechanical Engineers, Part C: Journal of Mechanical Engineering Science*, vol. 224, no. 7, pp. 1435–1454, 2010.

[5] S. Sokhanvar, J. Dargahi, S. Najarian, and S. Arbatani, *Tactile sensing and displays haptic feedback for minimally invasive surgery and robotics*. Chichester, West Sussex: Wiley, 2013.

[6] P. Saccomandi, E. Schena, C. Oddo, L. Zollo, S. Silvestri, and E. Guglielmelli, "Microfabricated tactile sensors for biomedical applications: A review," *Biosensors*, vol. 4, no. 4, pp. 422–448, 2014.

[7] L. Li, B. Yu, C. Yang, P. Vagdargi, R. A. Srivatsan, and H. Choset, "Development of an inexpensive tri-axial force sensor for minimally invasive surgery," in *2017 IEEE/RSJ International Conference on Intelligent Robots and Systems (IROS)*, 2017, pp. 906–913.

[8] U. Kim, Y. B. Kim, D.-Y. Seok, J. So, and H. R. Choi, "A surgical palpation probe with 6-axis force/torque sensing capability for minimally invasive surgery," *IEEE Transactions on Industrial Electronics*, vol. 65, no. 3, pp. 2755–2765, 2018.

[9] P. Regtien, *Sensors for Mechatronics*, ser. Elsevier Insights, 2012.

[10] J. Radó, C. Dücső, P. Földesy, G. Szebényi, H. Sántha, K. Rohr, L. Mucha, K. Lis, W. Sadowski, D. Krawczyk, P. Kroczek, Z. Malota, Z. Nawrat, and P. Füijes, "Force sensitive smart laparoscope of robin heart surgical robot," in *2018 Symposium on Design, Test, Integration Packaging of MEMS and MOEMS (DTIP)*, 2018, pp. 1–4.

[11] Y. Guo, J. Kong, H. Liu, H. Xiong, G. Li, and L. Qin, "A three-axis force fingertip sensor based on fiber bragg grating," *Sensors and Actuators A: Physical*, vol. 249, pp. 141–148, 2016.

[12] A. Taghipour, A. N. Cheema, X. Gu, and F. Janabi-Sharifi, "Temperature independent triaxial force and torque sensor for minimally invasive interventions," *IEEE/ASME Transactions on Mechatronics*, vol. 25, no. 1, pp. 449–459, 2020.

[13] C. Shi, M. Li, C. Lv, J. Li, and S. Wang, "A high-sensitivity fiber bragg grating-based distal force sensor for laparoscopic surgery," *IEEE Sensors Journal*, vol. 20, no. 5, pp. 2467–2475, 2020.

[14] A. Faragasso, J. Bimbo, Y. Noh, A. Jiang, S. Sareh, H. Liu, T. Nanayakkara, H. A. Wurdemann, and K. Althoefer, "Novel uniaxial force sensor based on visual information for minimally invasive surgery," in *IEEE International Conference on Robotics and Automation*, 2014, pp. 1405–1410.

[15] M. E. Giannaccini, S. Whyle, and N. F. Lepora, "Force sensing with a biomimetic fingertip," in *Biomimetic and Biohybrid Systems*, ser. Lecture Notes in Computer Science. Cham: Springer International Publishing, 2016, pp. 436–440.

[16] W. Yuan, S. Dong, and E. H. Adelson, "Gelsight: High-resolution robot tactile sensors for estimating geometry and force," *Sensors (Basel)*, vol. 17, no. 12, 2017.

[17] M. Goka, H. Nakamoto, and S. Takenawa, "A magnetic type tactile sensor by gmr elements and inductors," in *IEEE/RSJ International Conference on Intelligent Robots and Systems*, 2010, pp. 885–890.

[18] S. Youssefian, N. Rahbar, and E. Torres-Jara, "Contact behavior of soft spherical tactile sensors," *IEEE Sensors Journal*, vol. 14, no. 5, pp. 1435–1442, 2014.

[19] C. Ledermann, S. Wirges, D. Oertel, M. Mende, and H. Woern, "Tactile sensor on a magnetic basis using novel 3d hall sensor - first prototypes and results," in *IEEE International Conference on Intelligent Engineering Systems (INES)*, 2013, pp. 55–60.

[20] H. Wang, D. Jones, G. de Boer, J. Kow, L. Beccai, A. Alazmani, and P. Culmer, "Design and characterization of tri-axis soft inductive tactile sensors," *IEEE Sensors Journal*, vol. 18, pp. 7793–7801, 2018.

[21] C. G. Prattichizzo and Domenico, "A mathematical model of the pneumatic force sensor for robot-assisted surgery," *IEEE World Haptics Conference*, 2019.

[22] X. Zhang, J. Kow, D. Jones, G. de Boer, A. Ghanbari, A. Serjouei, P. Culmer, and A. Alazmani, "Adjustable compliance soft sensor via an elastically inflatable fluidic dome," *Sensors*, vol. 21, no. 6, 2021. [Online]. Available: https://www.mdpi.com/1424-8220/21/6/1970

[23] D. Raitt, S. Homer-Vanniasinkam, S. Abad Guaman, and H. Wurdemann, "Soft multimodal sensor with adjustable force sensing range for soft tissue palpation," in *Hamlyn Symposium on Medical Robotics*, 2021.

[24] J. Bewley, G. P. Jenkinson, and A. Tzemanaki, "Optical-tactile sensor for lump detection using pneumatic control," *Frontiers in Robotics and AI*, vol. 8, p. 199, 2021. [Online]. Available: https://www.frontiersin.org/article/10.3389/frobt.2021.672315

[25] A. Ali, K. Althoefer, and J. Konstantinova, "Dynamic response characteristics in variable stiffness soft inflatable links," in *Towards Autonomous Robotic Systems*, K. Althoefer, J. Konstantinova, and K. Zhang, Eds., 2019, pp. 160–170.

[26] "Open source computer vision library," https://opencv.org/, accessed: 2019-09-30.

[27] H. Takeishi, R. G. Baldovino, N. T. Bugtai, and E. P. Dadios, "A force sensing-based pneumatics for robotic surgery using neural network," in *2018 IEEE 10th International Conference on Humanoid, Nanotechnology, Information Technology,Communication and Control, Environment and Management (HNICEM)*, 2018, pp. 1–6.

[28] Z. Xu, Y. Zheng, and S. A. Rawashdeh, "A simple robotic fingertip sensor using imaging and shallow neural networks," *IEEE Sensors Journal*, vol. 19, no. 19, pp. 8878–8886, 2019.

[29] A. Padmanabha, F. Ebert, S. Tian, R. Calandra, C. Finn, and S. Levine, "Omnitact: A multi-directional high resolution touch sensor," 2020.

[30] L. He, Q. Lu, S. Abad, N. Rojas, and T. Nanayakkara, "Soft fingertips with tactile sensing and active deformation for robust grasping of delicate objects," *IEEE Robotics and Automation Letters*, vol. 5, no. 2, pp. 2714–2721, 2020.

Duncan G. Raitt received an MEng degree in mechanical engineering with international study from the University of Strathclyde, Glasgow, Scotland in 2019. He is currently pursuing a Ph.D. degree in mechanical engineering from UCL, London, UK. His main research interests include haptics and soft robotics.

Sara-Adela Abad received a BEng degree in electronic and control engineering from National Polytechnic School, Quito, Ecuador, an M.Sc. degree in artificial intelligence from the University of Southampton, Southampton, UK, and a Ph.D. degree in design engineering and robotics from Imperial College London, South Kensington, UK., in June 2019. She is a Research Fellow in soft robotics and haptics with the Mechanical Engineering Department, University College London. Her research interests include biologically inspired robots, soft robotics, and robots' adaptability to uncertain conditions.

Helge A Wurdemann is Associate Professor of Robotics at University College London leading the Soft Haptics and Robotics lab in the Department of Mechanical Engineering. Prior, he received a degree (Dipl.-Ing.) in electrical engineering with focus on mechatronics and robotics in the medical field from the Leibniz University of Hanover, and a PhD in Robotics from King's College London in 2012. Helge has authored over 100 articles, published in high-impact journals, and peer-reviewed full-length conference papers, presented at leading robotics conferences.

Shervanthi Homer-Vanniasinkam is a Consultant Vascular Surgeon at Leeds Teaching Hospitals NHS Trust, the Founding Professor of Surgery at the University of Warwick Medical School & University Hospitals Coventry and Warwickshire, and Professor of Engineering & Surgery at University College London. She has published over 150 papers and book chapters, delivered over 300 presentations and has a significant research grant portfolio with an outstanding track record of national and international collaborative research. She is a Visiting Scholar at Harvard University, the Yeoh Ghim Seng Visiting Professor of Surgery at the National University of Singapore and the Brahm Prakash Visiting Professor at the Indian Institute of Science.